An improved dynamic subgrid-scale model and its application to large eddy simulation of rotating channel flows

LIU Nansheng, LU Xiyun & ZHUANG Lixian

Department of Mechanics and Mechanical Engineering, University of Science and Technology of China, Hefei 230026, China
Correspondence should be addressed to Lu Xiyun (email: xlu@ustc.edu.cn)

Received January 12, 2004

Abstract A new dynamic subgrid-scale (SGS) model, which is proved to satisfy the principle of asymptotic material frame indifference (AMFI) for rotating turbulence, is proposed based on physical and mathematical analysis. Comparison with direct numerical simulation (DNS) results verifies that the new SGS model is effective for large eddy simulation (LES) on rotating turbulent flow. The SGS model is then applied to the LES of the spanwise rotating turbulent channel flow to investigate the rotation effect on turbulence characteristics, budget terms in the transport equations of resolved Reynolds stresses, and flow structures near the wall regions of the rotating channel.

Keywords: large eddy simulation (LES), dynamic subgrid-scale (SGS) model, rotating turbulent channel flow, *asymptotic material frame indifference (AMFI).*

DOI: 10.1360/03yw0228

Rotating turbulence occurs extensively in nature and engineering circumstances. Meanwhile, understanding physical mechanisms of the rotating turbulence is important to the fundamental research of turbulence. The turbulent flow in rotating frames undergoes two kinds of Coriolis force effects. First, a secondary flow is induced in the case that there is a mean vorticity component perpendicular to the rotating axis. Second, there are augmenting or suppressing effects on the turbulence if there is a mean vorticity component parallel to the rotating axis. Both the two effects profoundly affect not only the mean flow field, but also the turbulence intensities and coherent structures in the wall region. According to the Taylor-Proudman theorem, turbulence subject to strong rotation will undertake a transition toward the two-dimensional state and eventually to relaminarization, which is observed in experiments; thus the turbulence dissipation rate becomes trivial and the turbulent eddy viscosity vanishes, which represents the dependence of the turbulent eddy viscosity on the imposed rotation[1]. Meanwhile, the strong rotation suppresses the nonlinear energy cascade from large to small scales through phase scrambling[2]. Although the angular velocity of rotating frame disappears in the

transport equation of turbulent kinetic energy, it has been recognized that the rotation exhibits a significant influence on turbulence production and dissipation. However, some physical mechanism of rotating turbulent flow is still unclear and needs to be investigated further.

In the past decade, large eddy simulation (LES) method becomes an efficient tool for the prediction of complex turbulent flows. The rationale of this approach is to compute the large-scale components directly and model the subgrid scales via SGS model. So, a reasonable SGS model is crucial in the LES method. Extensive efforts have been taken to develop and improve the SGS model. Thus, the construction of reasonable SGS model, which can account for rotation effect on turbulent flow, is still a challenging problem.

Bradshaw[3] elucidated the similarity among the effects of rotation, streamline curvature and thermal stratification on turbulent flows and defined an equivalent gradient "Richardson number" to identify either an augmenting or suppressing effect on the flow subject to system rotation. Fu and Wang[4] proposed a second-moment closure modeling of turbulence in a non-inertial frame. Rubinstein and Zhou[5] constructed a SGS model by direct interaction approximation, which reproduces the fact that turbulent eddy viscosity vanishes in the limit case $\Omega \to \infty$. Unfortunately, the model coefficients in those models are determined empirically.

For turbulent flow in rotating frame, Speziale[6—8] indicated that the SGS stress tensor formation is dependent on the frame of reference but the divergence of SGS stress tensor is independent of the frame of reference, and required that the SGS model should be compatible with the principle of material frame indifference (MFI). Shimomura et al.[9,10] further claimed that the principle of MFI should be imposed not only on the divergence of SGS stress tensor but also on the SGS stress tensor itself in the limit of $\Omega \to \infty$, where Ω is the angular velocity of the reference frame. This constraint requires that the dependence of the model equation for the SGS stress tensor tends to disappear as Ω approaches infinity, which is referred to as the asymptotic material frame indifference (AMFI) of the SGS model equation. The principle of AMFI is theoretically proved and regarded as a constraint to the SGS stress closures for rotating turbulent flow. By examining some typical SGS models, it is found that most SGS models, e.g. Smagorinsky model[11], dynamic Smagorinsky model[12] and dynamic mixing model[13], are inconsistent with the principle of AMFI. Thus, the motivation of this study is to develop a reasonable SGS model that is consistent with the principle of AMFI and accounts for the influence of the system rotation on the turbulent flow.

In this study, a nonlinear SGS model satisfying the principle of AMFI is proposed, whose coefficients are dynamically determined based on the resolved flow field. The performance of the nonlinear SGS model is examined by the LES of the spanwise rotating turbulent channel flow. Then, the rotation effect on turbulence characteristics is investigated.

1 Mathematical formulation

The governing equations for the LES of the spanwise rotating turbulent channel flow (as shown in fig. 1 for the sketch) are the three-dimensional filtered Navier-Stokes equations. To non-dimensionalize the governing equations, the friction velocity u_τ is used as the velocity scale, and the half-height of the channel h as the length scale. The non-dimensional governing equations are given as

$$\frac{\partial \overline{u}_i}{\partial x_i} = 0, \tag{1}$$

$$\frac{\partial \overline{u}_i}{\partial t} + \frac{\partial \overline{u}_i \overline{u}_j}{\partial x_j} = -\frac{\partial \overline{p}}{\partial x_i} - \delta_{1i} + \frac{1}{\mathrm{Re}_\tau} \frac{\partial^2 \overline{u}_i}{\partial x_j \partial x_j} - N_\tau \varepsilon_{ijk} \frac{\Omega_j}{\Omega} \overline{u}_k - \frac{\partial \tau_{ij}}{\partial x_j}, \tag{2}$$

where the overbar denotes the resolved variable, $\overline{p}$ is the sum of the pressure and centrifugal force. The non-dimensional parameters in this problem are the rotation number and Reynolds number, which are defined as $N_\tau = 2\Omega h / u_\tau$ and $\mathrm{Re}_\tau = u_\tau h / \nu$, respectively. $\overline{u}_i$ $(i = 1, 2, 3)$ is the resolved velocity and is represented as, for writing convenience, u, v and w in the streamwise (x_1, or x), wall-normal (x_2, or y) and spanwise (z, or x_3) directions in rotating Cartesian coordinate system. In eq. (2), $\tau_{ij} = \overline{u_i u_j} - \overline{u}_i \overline{u}_j$ is the subgrid-scale turbulent stress and needs to be modeled by SGS model.

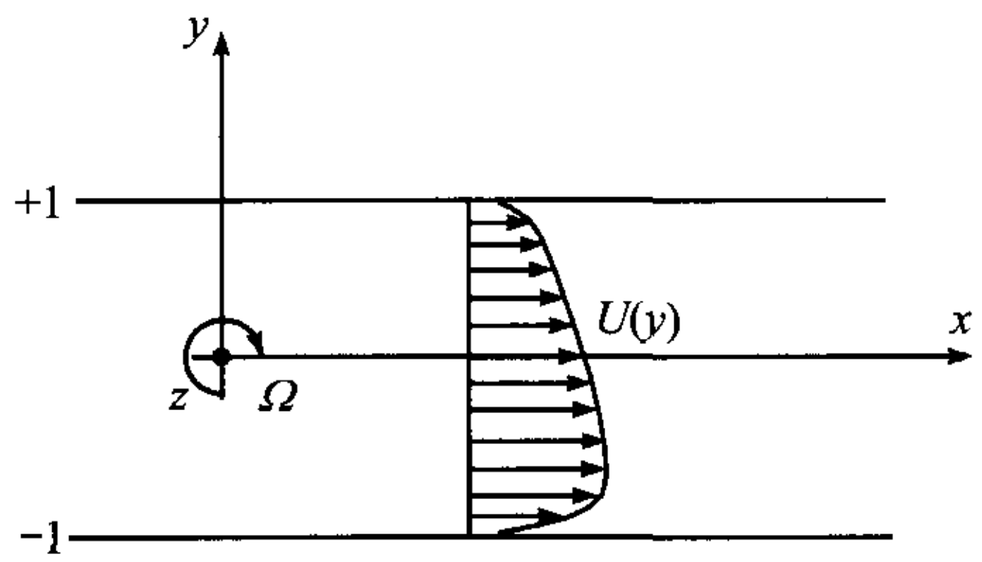

Fig. 1. Sketch of the spanwise rotating turbulent channel.

2 Nonlinear dynamic SGS model for rotating turbulence

2.1 Nonlinear SGS model functional form in inertial frame

To specify the model's functional form, we neglect the turbulence historical effects and assume that τ_{ij} depends instantaneously on local $\partial \overline{u}_i / \partial x_j$ and some scalars. Under this hypothesis, τ_{ij} can be written in the following functional form:

$$\tau_{ij} = F\left(\frac{\partial \overline{u}_i}{\partial x_j}, S\right), \tag{3}$$

where S represents a scalar group and will appear in the coefficients of the model. Here, we further decompose $\partial \overline{u}_i / \partial x_j$ into strain tensor $\overline{s}_{ij}$ and rotation tensor $\overline{\omega}_{ij}$,

$$\bar{s}_{ij} = \frac{1}{2}\left(\frac{\partial \bar{u}_i}{\partial x_j} + \frac{\partial \bar{u}_j}{\partial x_i}\right), \quad \bar{\omega}_{ij} = \frac{1}{2}\left(\frac{\partial \bar{u}_j}{\partial x_i} - \frac{\partial \bar{u}_i}{\partial x_j}\right). \tag{4}$$

Then, based on the tensor operation rule, an asymptotic expansion on eq. (3) about $\bar{s}_{ij}$ and $\bar{\omega}_{ij}$ is taken. The symmetric tensor τ_{ij} thus can be written as

$$\begin{aligned}\tau_{ij} - \frac{1}{3}\tau_{kk}\delta_{ij} = &-2\nu_a \bar{s}_{ij} + \nu_b(\bar{s}_{ik}\bar{\omega}_{kj} + \bar{s}_{jk}\bar{\omega}_{ki}) \\ &+ \nu_c\left(\bar{s}_{ik}\bar{s}_{kj} - \frac{1}{3}\bar{s}_{kl}\bar{s}_{kl}\delta_{ij}\right) + \nu_d\left(\bar{\omega}_{ik}\bar{\omega}_{kj} - \frac{1}{3}\bar{\omega}_{lk}\bar{\omega}_{kl}\delta_{ij}\right).\end{aligned} \tag{5}$$

Compared to the second-order SGS model proposed by Kosovic[14], this nonlinear SGS model is of perfect functional form, which contains all the second-order nonlinear terms of $\bar{s}_{ij}$ and $\bar{\omega}_{ij}$. In an inertial frame, the effect of the system rotation on τ_{ij} is represented implicitly by $\bar{s}_{ij}$ and $\bar{\omega}_{ij}$.

2.2 Nonlinear SGS model functional form in rotating frame

Further, it is needed to deduce the functional form of the nonlinear SGS model in non-inertial frame. By taking orthogonal rotational frame transform on eq. (5), the nonlinear SGS model functional form in rotating frame is then written as

$$\begin{aligned}(\tau_{ij}^*)_\Sigma = &-2\nu_a'\bar{\Delta}^2 |\bar{s}^*| \bar{s}_{ij}^* + \nu_b'\frac{\bar{\Delta}^2}{12}(\bar{s}_{ik}^*\bar{\omega}_{kj}^* + \bar{s}_{jk}^*\bar{\omega}_{ki}^*) + \nu_b'\frac{\bar{\Delta}^2}{12}\left(\bar{\omega}_{ik}^*\bar{\omega}_{kj}^* - \frac{1}{3}\delta_{ij}\bar{\omega}_{lk}^*\bar{\omega}_{kl}^*\right) \\ &+\nu_c'\bar{\Delta}^2\left(\bar{s}_{ik}^*\bar{s}_{kj}^* - \frac{1}{3}\delta_{ij}\bar{s}_{kl}^*\bar{s}_{kl}^*\right) + (\nu_b' - 1)\left(Z_{ij}^* - \frac{1}{3}\delta_{ij}Z_{kk}^*\right).\end{aligned} \tag{6}$$

This form is proved to satisfy the principle of AMFI. In eq. (6), the superscript '*' denotes the variable in rotating coordinate system. $(f_{ij})_\Sigma = f_{ij} - \delta_{ij}f_{kk}/3$; ν_a', ν_b' and ν_c' are non-dimensional model coefficients and are represented as $\nu_a = \bar{\Delta}^2\nu_a'|\bar{s}^*|$, $\nu_b = \bar{\Delta}^2\nu_b'/12$ and $\nu_c = \bar{\Delta}^2\nu_c'$, respectively; $|\bar{s}^*| = (\bar{s}_{ij}^*\bar{s}_{ij}^*)^{1/2}$; $\bar{\Delta}$ is the grid filter size; Z_{ij}^* is the additional tensor due to the orthogonal rotational frame transform

$$Z_{ij}^* = \frac{\bar{\Delta}^2}{12}\left(\varepsilon_{iab}\Omega_a^*\frac{\partial\overline{u_j^*}}{\partial x_b^*} + \varepsilon_{jab}\Omega_a^*\frac{\partial\overline{u_i^*}}{\partial x_b^*} + \delta_{ij}\Omega_a^*\Omega_a^* - \Omega_i^*\Omega_j^*\right), \tag{7}$$

which indicates that τ_{ij}^* is the function of the angular velocity $\boldsymbol{\Omega}$ of the rotating frame. Then, the nonlinear SGS model in the inertial frame can be rewritten as

$$(\tau_{ij})_\Sigma = -2\nu_a'\overline{\Delta}^2 \mid \overline{s} \mid \overline{s}_{ij} + \nu_b' \frac{\overline{\Delta}^2}{12}(\overline{s}_{ik}\overline{\omega}_{kj} + \overline{s}_{jk}\overline{\omega}_{ki})$$

$$+ \nu_b' \frac{\overline{\Delta}^2}{12}\left(\overline{\omega}_{ik}\overline{\omega}_{kj} - \frac{1}{3}\delta_{ij}\overline{\omega}_{lk}\overline{\omega}_{kl}\right) + \nu_c'\overline{\Delta}^2\left(\overline{s}_{ik}\overline{s}_{kj} - \frac{1}{3}\delta_{ij}\overline{s}_{kl}\overline{s}_{kl}\right). \quad (8)$$

Detailed derivation can be found in footnote 1) and is thus omitted here. In this study, LES is carried out in the rotating frame. So, the nonlinear SGS model functional form (6) is used to model the SGS stress.

2.3 Determination of the coefficients in the nonlinear SGS model

According to the dynamic procedure proposed by Germano et al.[12] to determine the model coefficients, the test-filtered SGS stress in rotating coordinates T_{ij}^* can be modeled by a functional form similar to eq. (6):

$$(T_{ij}^*)_\Sigma = -2\nu_a'\hat{\overline{\Delta}}^2 \mid \hat{\overline{s}}^* \mid \hat{\overline{s}}_{ij}^* + \nu_b' \frac{\hat{\overline{\Delta}}^2}{12}(\hat{\overline{s}}_{ik}^*\hat{\overline{\omega}}_{kj}^* + \hat{\overline{s}}_{jk}^*\hat{\overline{\omega}}_{ki}^*) + \nu_b' \frac{\hat{\overline{\Delta}}^2}{12}\left(\hat{\overline{\omega}}_{ik}^*\hat{\overline{\omega}}_{kj}^* - \frac{1}{3}\delta_{ij}\hat{\overline{\omega}}_{lk}^*\hat{\overline{\omega}}_{kl}^*\right)$$

$$+ \nu_c'\hat{\overline{\Delta}}^2\left(\hat{\overline{s}}_{ik}^*\hat{\overline{s}}_{kj}^* - \frac{1}{3}\delta_{ij}\hat{\overline{s}}_{kl}^*\hat{\overline{s}}_{kl}^*\right) + (\nu_b' - 1)(\hat{Z}_{ij}^*)_\Sigma, \quad (9)$$

where the superscript '^' denotes the test-filtered variable, and Δ is the test filter size.

Substituting eqs. (6) and (9) into the Leonard stress, i.e. $L_{ij}^* = \hat{\overline{u}}_i^*\hat{\overline{u}}_j^* - \hat{\overline{u}}_i^*\hat{\overline{u}}_j^* = T_{ij}^* - \hat{\tau}_{ij}^*$, we then obtain

$$K_{ij} = \nu_a' A_{ij} + \nu_b' B_{ij} + \nu_c' C_{ij}, \quad (10)$$

where

$$K_{ij} = \hat{\overline{u}}_i^*\hat{\overline{u}}_j^* - \hat{\overline{u}}_i^*\hat{\overline{u}}_j^* + \left(1 - \frac{\overline{\Delta}^2}{\hat{\overline{\Delta}}^2}\right)(\hat{Z}_{ij}^*)_\Sigma, \quad A_{ij} = 2\overline{\Delta}^2 \mid \hat{\overline{s}}^* \mid \hat{\overline{s}}_{ij}^* - 2\hat{\overline{\Delta}}^2 \mid \hat{\overline{s}}^* \mid \hat{\overline{s}}_{ij}^*,$$

$$B_{ij} = -\frac{\overline{\Delta}^2}{12}(\hat{\overline{s}}_{ik}^*\hat{\overline{\omega}}_{kj}^* + \hat{\overline{s}}_{jk}^*\hat{\overline{\omega}}_{ki}^*) + \frac{\hat{\overline{\Delta}}^2}{12}(\hat{\overline{s}}_{ik}^*\hat{\overline{\omega}}_{kj}^* + \hat{\overline{s}}_{jk}^*\hat{\overline{\omega}}_{ki}^*) - \frac{\overline{\Delta}^2}{12}\left(\hat{\overline{\omega}}_{ik}^*\hat{\overline{\omega}}_{kj}^* - \frac{1}{3}\delta_{ij}\hat{\overline{\omega}}_{lk}^*\hat{\overline{\omega}}_{kl}^*\right)$$

$$+ \frac{\hat{\overline{\Delta}}^2}{12}\left(\hat{\overline{\omega}}_{ik}^*\hat{\overline{\omega}}_{kj}^* - \frac{1}{3}\delta_{ij}\hat{\overline{\omega}}_{lk}^*\hat{\overline{\omega}}_{kl}^*\right) + \left(1 - \frac{\overline{\Delta}^2}{\hat{\overline{\Delta}}^2}\right)(\hat{Z}_{ij}^*)_\Sigma,$$

---

1) Liu Nansheng, Direct numerical and large eddy simulations on rotating turbulence, Dissertation of University of Science and Technology of China, 2003.

$$C_{ij} = -\bar{\Delta}^2 \left(\overline{\bar{s}_{ik}^* \hat{\bar{s}}_{kj}^*} - \frac{1}{3}\delta_{ij} \overline{\bar{s}_{kl}^* \hat{\bar{s}}_{kl}^*} \right) + \hat{\bar{\Delta}}^2 \left(\hat{\bar{s}}_{ik}^* \hat{\bar{s}}_{kj}^* - \frac{1}{3}\delta_{ij} \hat{\bar{s}}_{kl}^* \hat{\bar{s}}_{kl}^* \right).$$

According to Lilly's proposal[15], the model coefficients, ν_a', ν_b' and ν_c', can be determined in a least-square method[1)]. It is proved that, as $|\boldsymbol{\Omega}| \to \infty$, $\nu_a' \sim O(1)$, $\nu_b' - 1 \to O(1/\Omega^2)$, $\nu_c' \sim O(1)$. So, the functional form of the nonlinear SGS model in eq. (6) is independent of Ω in the limit case $|\boldsymbol{\Omega}| \to \infty$; it means that the model satisfies the principle of AMFI.

3 Numerical method

To perform LES calculation, the factional-step method, developed by Rai and Moin[16] and Kim and Moin[17], was employed to solve the filtered Navier-Stokes equations. Spatial derivatives are discretized by a second order central difference. The convective and viscous terms are treated by Adams-Bashforth and Crank-Nicholson schemes, respectively, and a third order Runge-Kutta scheme is used to advance in time through three sub-steps.

By use of the nonlinear SGS model described above, the LES is carried out for the spanwise rotating turbulent channel flow. Periodic boundary conditions are imposed in the streamwise and spanwise directions, no-slip and no-penetration conditions are employed on the walls of the channel. The channel flow is driven by a constant pressure gradient in the streamwise direction.

4 Results and discussion

Here, fully developed turbulent flow is through a channel that is assumed to rotate in the clockwise direction with the rotating axis along the spanwise direction at an angular velocity $\boldsymbol{\Omega}$ (as shown in fig. 1). The Reynolds number is $\mathrm{Re}_\tau = 194$ and the rotation number $N = 0.1$—0.5, which is defined as $N = 2\Omega h/U_m$, U_m is the bulk mean velocity. The computational domain is $4\ \pi h \times 2\ h \times 2\ \pi h$ in the streamwise, wall-normal and spanwise directions, respectively, and is resolved by the corresponding grid size $97 \times 81 \times 65$ with uniform grid in the streamwise and spanwise directions and stretched grid in the wall-normal direction. To achieve a high resolution, five grid points are located in the wall regions within $y^+ < 10$. According to the present and previous DNS data[18,19], both the computational domain size and grid number are sufficient.

Following the terminology[20,21], the lower wall and the upper wall of the rotating channel are termed suction wall and pressure wall. In addition, the DNS performed by Kristoffersen et al.[19] and the present DNS and LES are represented as DNS-1, DNS-2 and NSM, respectively.

---

1) See footnote 1) on page 467.

4.1 Validation of nonlinear SGS model

Figs. 2 and 3 show the profiles of mean velocity and turbulence intensities in the rotating channel. Here, the mean velocity $\langle \overline{u}_i \rangle$ is the ensemble average of the resolved velocity $\overline{u}_i$, and the corresponding velocity fluctuation is calculated by $\overline{u}_i' = \overline{u}_i - \langle \overline{u}_i \rangle$. Comparisons are taken among the results of DNS-1, DNS-2 and NSM for N = 0.1, 0.2 and 0.5. As shown in fig. 2, although the mean velocity of NSM is slightly smaller than that of DNS, these profiles of $\langle \overline{u}_i \rangle$ are compatible with each other.

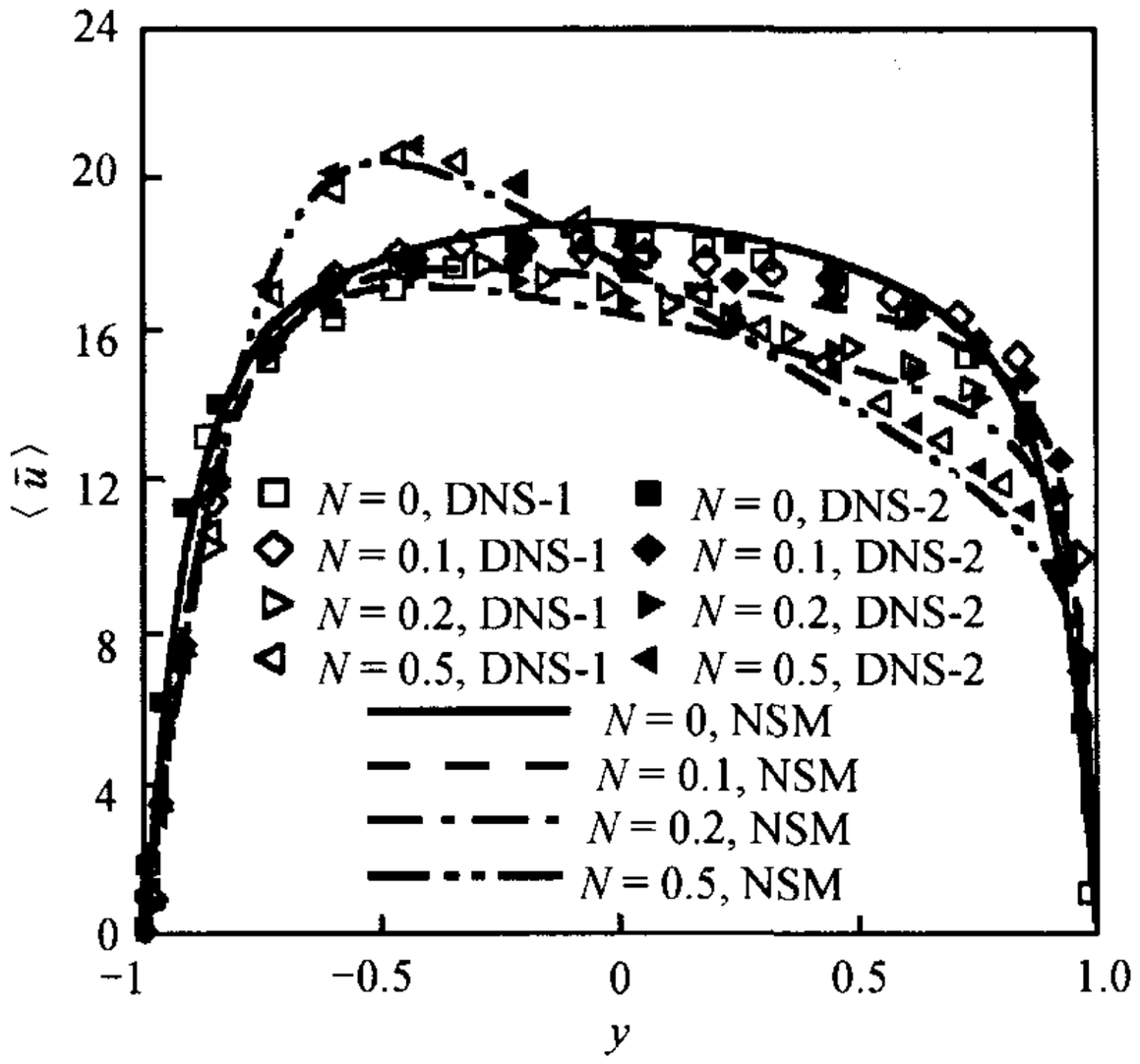

Fig. 2. Streamwise mean velocity profiles.

Fig. 3(a) and (b) show the profiles of the streamwise turbulence intensities. Near the pressure wall, $\langle \overline{u}'_{rms} \rangle$ predicted by NSM is in good agreement with those of DNS-1 and DNS-2. Near the suction wall, $\langle \overline{u}'_{rms} \rangle$ of NSM is slightly larger than the DNS results. Globally, the NSM results agree well with the DNS data. In fig. 3(c) and (d) the distributions of $\langle \overline{v}'_{rms} \rangle$ and $\langle \overline{w}'_{rms} \rangle$ calculated by the LES and DNS agree well over the channel.

Moreover, we have compared other turbulent quantities with the DNS results and can confirm that the present LES coupled with the nonlinear SGS model is able to predict turbulence characteristics of the rotating turbulent flow. Further, turbulence statistics and turbulence production and dissipation rates near the walls of the rotating channel are analyzed in the following.

4.2 Skewness and flatness factors

Figs. 4 and 5 show the profiles of the skewness and flatness of the streamwise and wall-normal velocity fluctuations, respectively. The skewness factor S and flatness factor F can be viewed as the measurement of extent to which the probability density function of turbulence fluctuation deviates from normal distribution. For Gaussian distribution, S = 0 and F = 3. Thus, the fact that $S(\overline{u}_i') < 0$ indicates that the velocity fluctuation with $\overline{u}_i' < 0$ is dominant in probability; otherwise, the velocity fluctuation with $\overline{u}_i' > 0$ becomes dominant. And the flatness factor represents the intermittent character of wall turbulence. Compared to the non-rotating case, both $S(\overline{u}')$ and $S(\overline{v}')$ near the suction wall are strengthened in fig. 4. The fact that $S(\overline{u}') > 0$ and $S(\overline{v}') < 0$ indicates that the main contribution to $\overline{u}'$ comes from the sweep events, which are related to the

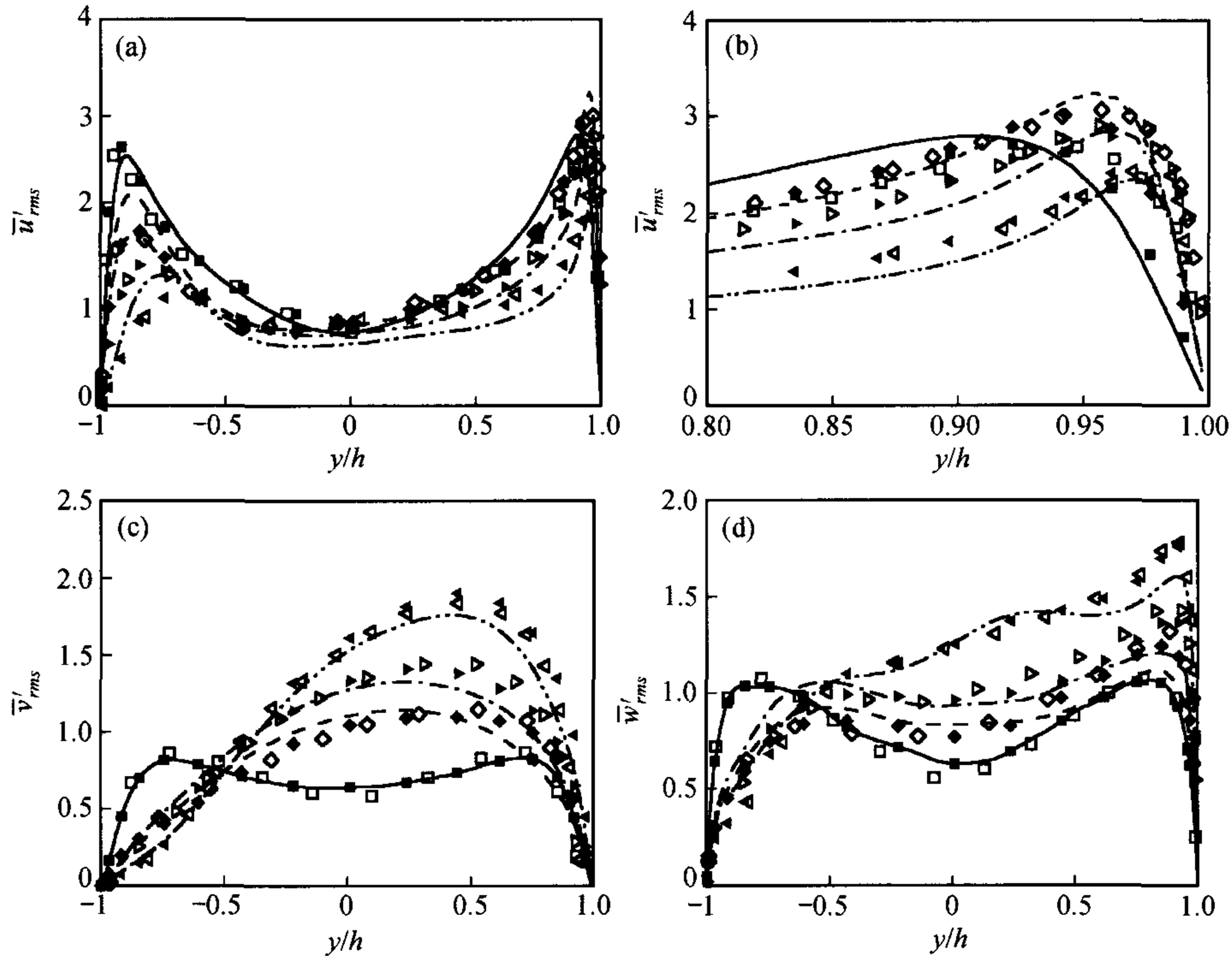

Fig. 3. Distributions of the root-mean-square values of velocity fluctuations. (a) Streamwise component; (b) local drawing of the streamwise component near the pressure wall; (c) wall-normal component; (d) spanwise component. All legends are the same as fig. 2.

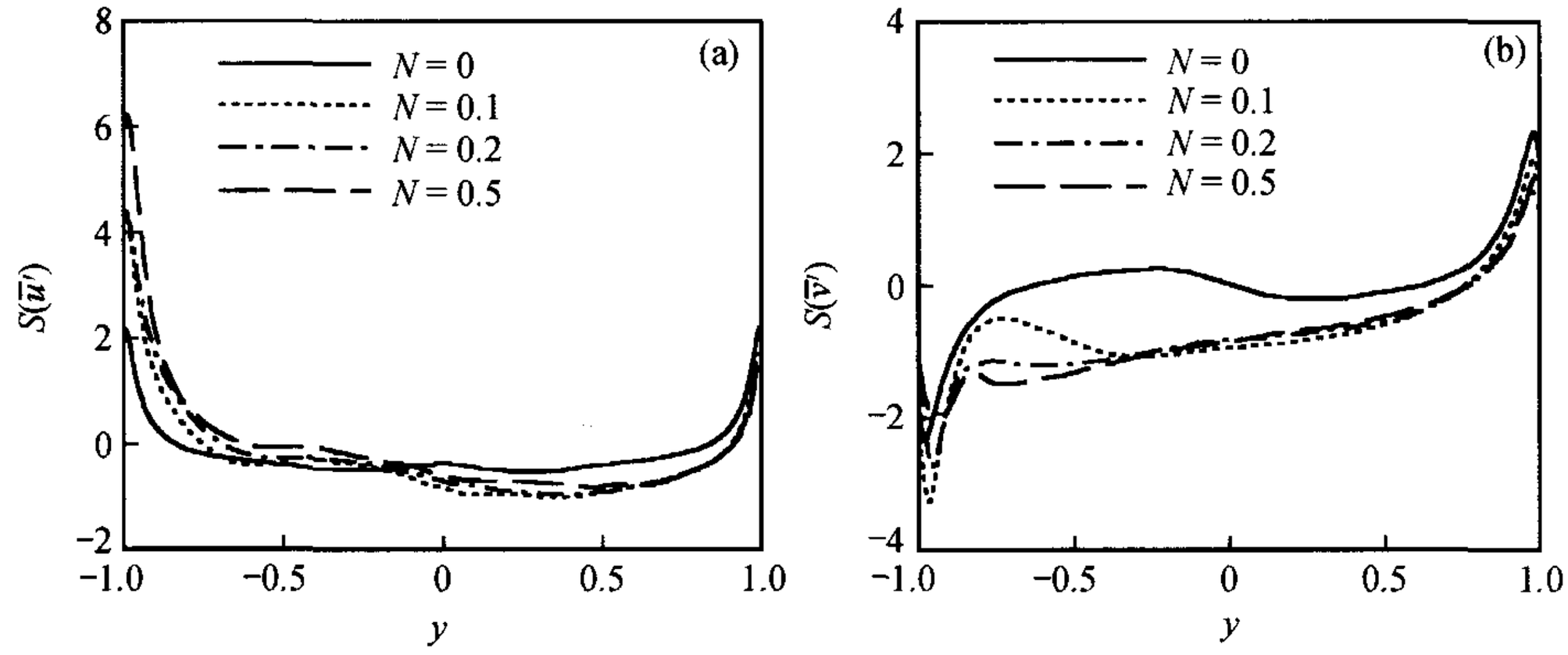

Fig. 4. Profiles of the skewness of velocity fluctuations. (a) Streamwise; (b) wall-normal.

high-speed elongated streaks. Similar behavior near the pressure wall is also found since $S(\overline{u}')>0$ and $S(\overline{v}')>0$. Fig. 5 shows that $F(\overline{u}')$ and $F(\overline{v}')$ increase near the suction wall for the rotating case; it is evident that turbulence becomes highly intermittent. However, the turbulence intermittent behavior becomes weak near the pressure wall. It is needed to note that $S(\overline{v}')$ and $F(\overline{v}')$ near the suction wall do not vary monotonically with the rotation number. This fact was also revealed for turbulent rotating pipe

flow based on DNS results and can be explained as the inclination of near-wall vortical structures induced by the rotation effect[22].

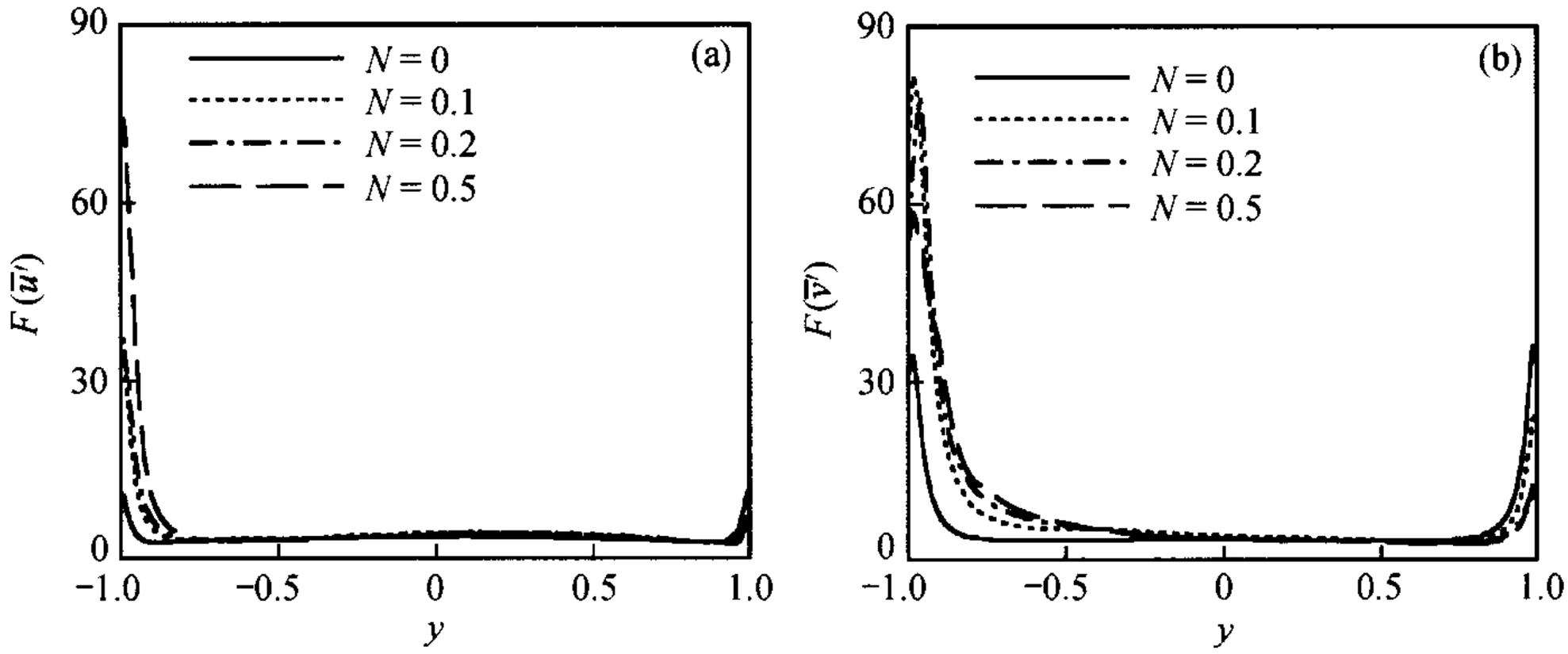

Fig. 5. Profiles of the flatness of velocity fluctuations. (a) Streamwise; (b) wall-normal.

4.3 Budgets of resolved Reynolds stresses

The resolved Reynolds stress budgets provide the detailed information of rotation effect on the dynamical characteristics of turbulence, e.g. production and dissipation rate of turbulent kinetic energy, redistribution of turbulent kinetic energy due to Coriolis force, and viscous and turbulent diffusion of resolved scale motions near the walls. By taking ensemble average on eq. (2), the transport equation of resolved Reynolds stresses can be obtained and written as

$$\frac{\partial\langle\overline{u}_i'\,\overline{u}_j'\rangle}{\partial t}=-\left(\langle\overline{u}_i'\,\overline{u}_k'\rangle\frac{\partial\langle\overline{u}_j\rangle}{\partial x_k}+\langle\overline{u}_j'\,\overline{u}_k'\rangle\frac{\partial\langle\overline{u}_i\rangle}{\partial x_k}\right)-\frac{\partial\langle\overline{u}_i'\,\overline{u}_j'\,\overline{u}_k'\rangle}{\partial x_k}$$

$$-\left\langle\overline{u}_i'\frac{\partial P'}{\partial x_j}+\overline{u}_j'\frac{\partial P'}{\partial x_i}\right\rangle+\left\langle\frac{\partial}{\partial x_k}\left[(\mathrm{Re}_\tau\nu_a+1)\frac{\partial\,\overline{u}_i'\,\overline{u}_j'}{\partial x_k}\right]\right\rangle-2\left\langle(\mathrm{Re}_\tau\nu_a+1)\frac{\partial\,\overline{u}_i'}{\partial x_k}\frac{\partial\,\overline{u}_j'}{\partial x_k}\right\rangle$$

$$-N_\tau\Omega_l\left(\varepsilon_{ilk}\langle\overline{u}_k'\,\overline{u}_j'\rangle+\varepsilon_{jlk}\langle\overline{u}_k'\,\overline{u}_i'\rangle\right)/\Omega+H_{ij}\,, \tag{11}$$

where ν_a is the eddy viscosity, P' is the modified pressure fluctuation $P'=\overline{p}'+\tau_{kk}'\delta_{ij}/3$. Eq. (11) is normalized by the velocity scale proposed by Mansour et al.[23] These terms on the right-hand side of eq. (11) are the production rate (P_{ij}, referred to as PR), turbulent diffusion (T_{ij}, TD), velocity-pressure correlation (VPG), viscous diffusion (D_{ij}, VD), dissipation rate (ε_{ij}, DS), Coriolis force term (N_{ij}, CO), and H_{ij} being the convection term of mean flow and the additional terms due to the nonlinear SGS model. Here, the VPG term can be further decomposed into the pressure-velocity diffusion (Π_{ij}, PV) and the pressure-strain correlation (π_{ij}, PS),

$$\Pi_{ij} = -\left\langle \frac{\partial(P'\overline{u}_i')}{\partial x_j} + \frac{\partial(P'\overline{u}_j')}{\partial x_i} \right\rangle, \qquad \pi_{ij} = \left\langle P'\left(\frac{\partial \overline{u}_i'}{\partial x_j} + \frac{\partial \overline{u}_j'}{\partial x_i} \right) \right\rangle. \tag{13}$$

Fig. 6 shows the profiles of the budget terms in the $\langle \overline{u}_2' \overline{u}_2' \rangle$ equation. In fig. 6(a), all the terms in the $\langle \overline{u}_2' \overline{u}_2' \rangle$ equation are suppressed strongly in the region of $y^+ < 10$ (i.e. near the suction wall), and only the PV and PS terms are dominant there. The CO term with positive value in most part of the rotating channel plays as a source term to $\langle \overline{u}_2' \overline{u}_2' \rangle$ and redistributes turbulent kinetic energy from the horizontal components to the wall-normal component. In fig. 6(b), it is evident that the redistribution of turbulence energy is more activated in the core region of the channel. Fig. 6(a) and (b) show that the TD term plays an important role to the $\langle \overline{u}_2' \overline{u}_2' \rangle$ budget in the core region of the channel, and the TD term is enhanced in the pressure wall region while suppressed in the suction wall region due to the system rotation effect.

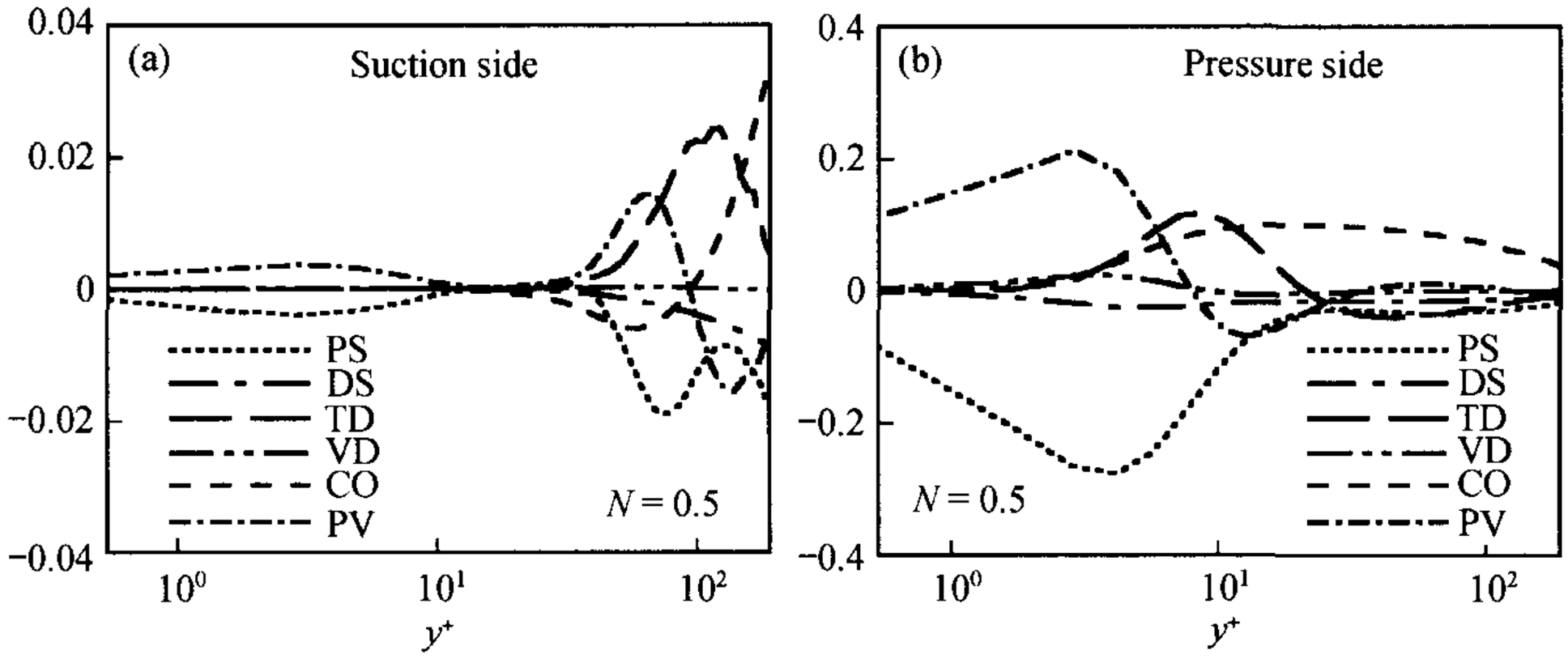

Fig. 6. Profiles of the budget terms in the $\langle \overline{u}_2' \overline{u}_2' \rangle$ equation at N = 0.5. (a) Near the suction wall; (b) near the pressure wall. $y^+ = (1 - |y|)\mathrm{Re}_\tau$.

Fig. 7 exhibits the profiles of the budget terms in the $\langle \overline{u}_1' \overline{u}_1' \rangle$ equation. In fig. 7(a), the peak of the PR term is damped near the suction wall and the position of the peak shifts away from the suction wall of the channel. The most intensive turbulence production is located at $y^+ \approx 45$, where the contributions of all these terms in the $\langle \overline{u}_1' \overline{u}_1' \rangle$ equation are comparable. Compared to the non-rotating channel flow, it is located at $y^+ \approx 12$ [17]. Fig. 7(b) shows that the PR term is strengthened near the pressure wall. The peak of the PR term is located at $y^+ \approx 5.2$, where the balance of the $\langle \overline{u}_1' \overline{u}_1' \rangle$ budget is achieved by the interaction of the PR, DS, VD and TD terms. It is evident (fig. 7(a), (b)) that the contributions of the VD and DS terms are dominant to the $\langle \overline{u}_1' \overline{u}_1' \rangle$ budget. Even though the CO term contributes little to the $\langle \overline{u}_1' \overline{u}_1' \rangle$ budget, it plays an important role in redistributing the turbulent kinetic energy near the wall regions. In

most region of the rotating channel, the CO term with negative value drains turbulence energy from the streamwise fluctuation to the wall-normal component.

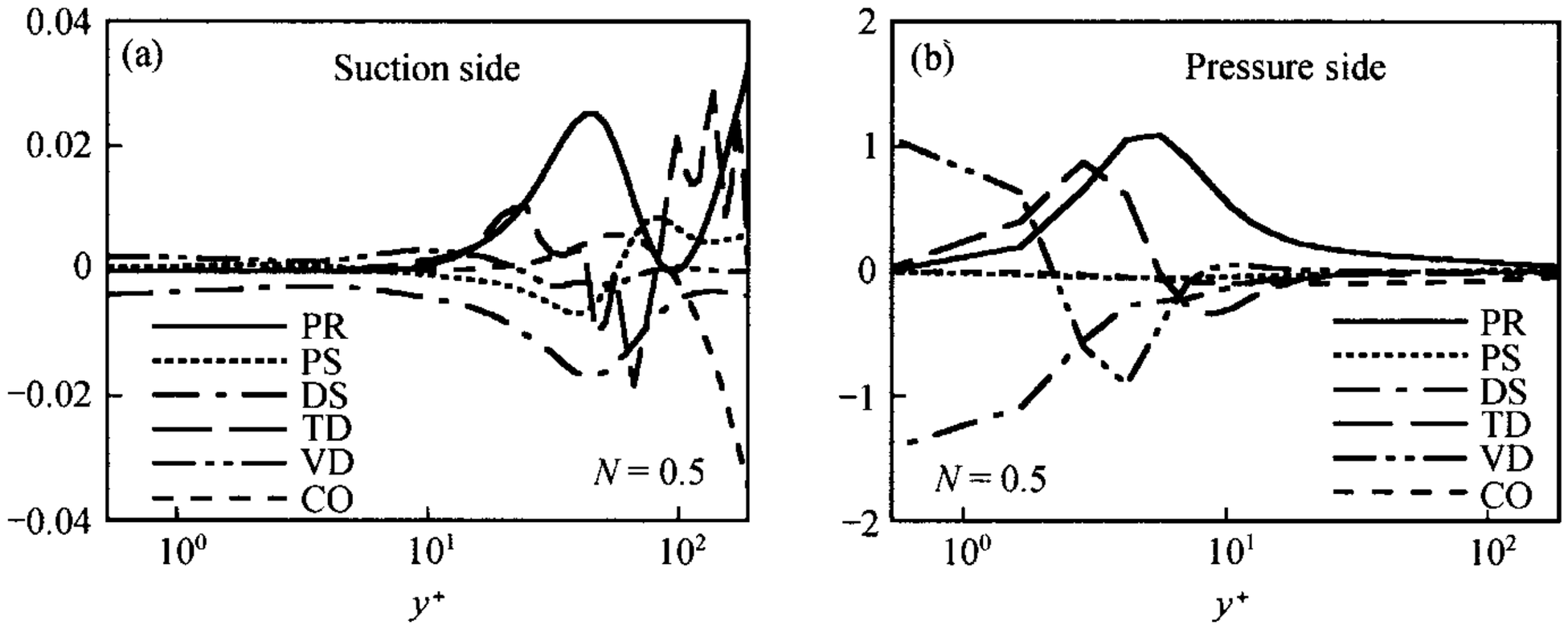

Fig. 7. Profiles of the budget terms in the $\langle \overline{u}_1' \overline{u}_1 \rangle$ equation at $N = 0.5$. (a) Near the suction wall; (b) near the pressure wall.

4.4 Flow structures

Coherent structures always get much attention in the study of wall turbulence, since the turbulence wall structures are responsible for the burst events, turbulence production and dissipation in turbulent boundary layer. Based on the patterns of near-wall velocity and vorticity fluctuations, Kim and Moin[17] investigated the coherent structures near the wall, e.g. elongated high- and low-speed streaks, sweep and ejection events. The flow structures predicted by the numerical simulation[17] are quite similar to those observed in experiment performed by Runstadler[24]. For the spanwise rotating turbulent channel flow, since turbulence intensity is enhanced near the pressure wall and suppressed near the suction wall, the flow structures near the walls will change due to the rotation effect correspondingly.

Fig. 8 shows the contours of the wall-normal velocity fluctuation $\overline{u}_2'$ in the (y^+, z^+) plane near the pressure and suction walls at $N = 0.5$. Compared to the non-rotating flow structure (not shown here), the velocity fluctuation $\overline{u}_2'$ shown in fig. 8(a) becomes more intensive, which indicates that the wall-normal turbulence intensity is enhanced near the pressure wall. Since the contours of $\overline{u}_2'$ with positive and negative values are related to the in-rush and out-rush motions, respectively, it is indicated in fig. 8(a) that turbulence sweep and ejection events become more active near the pressure wall. In the region between the positive and negative values of $\overline{u}_2'$, the Helmholtz instability of the shear layer appears, which is responsible for the generation of the streamwise vortical structures in the pressure wall region. According to fig. 8(b), the turbulence energy production, the sweep and ejection events are suppressed near the suction wall. The flow patterns with absent streaky structures are well consistent with the suppression of the production of the streamwise vortices.

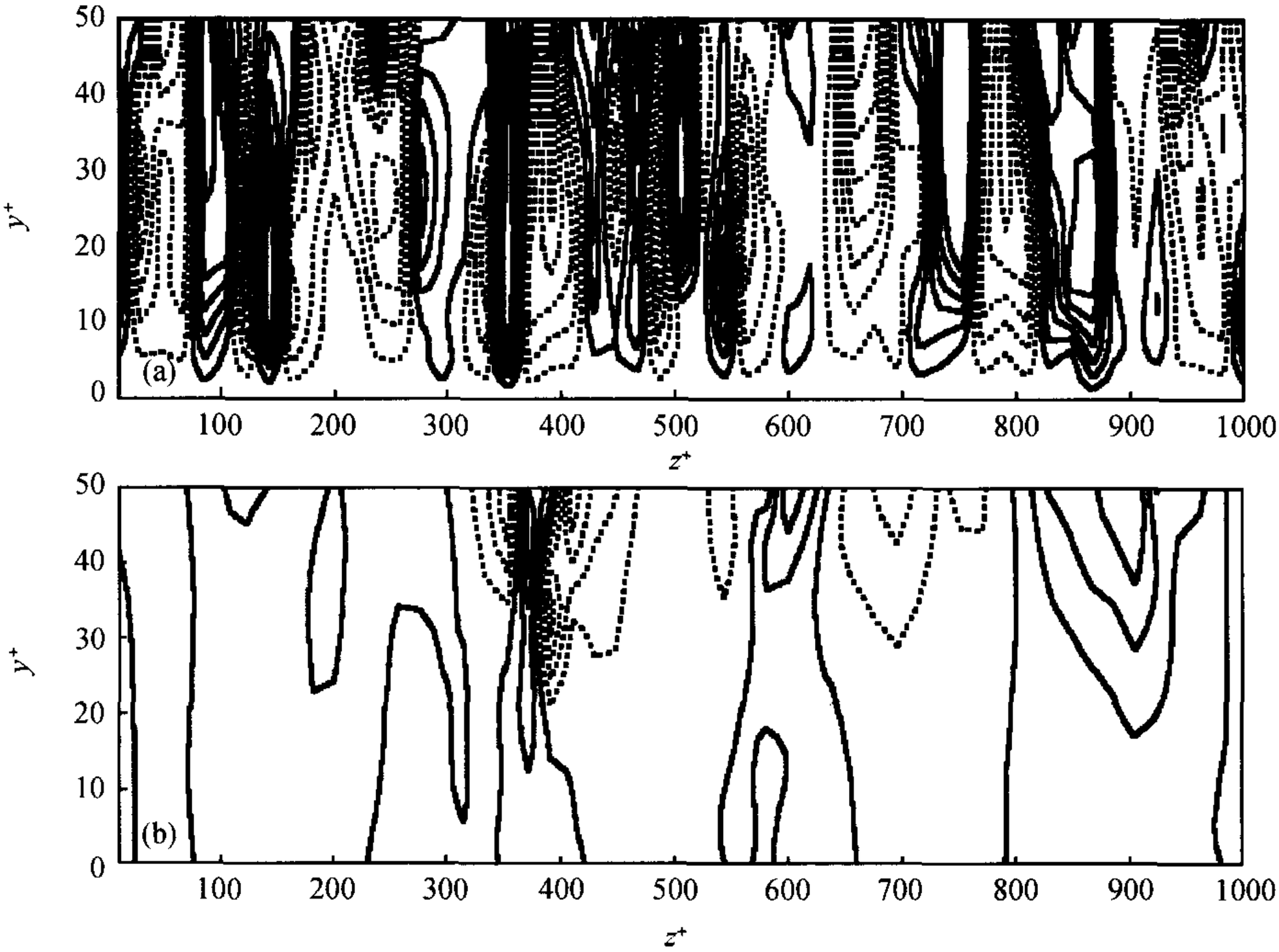

Fig. 8. Contours of the wall-normal velocity fluctuation in the y^+–z^+ plane at $N = 0.5$ with the increment of contour 0.2. (a) Near the pressure wall; (b) near the suction wall.

Fig. 9 depicts the contours of the streamwise velocity fluctuation $\overline{u}_1'$ in the same plane as shown in fig. 8. The contours of $\overline{u}_1'$ with positive and negative values are arranged alternately along the spanwise direction in fig. 9(a). Based on figs. 8(a) and 9(a), it is found that the positive $\overline{u}_1'$ is mostly related to the positive $\overline{u}_2'$, which corresponds to the flow rushing towards the pressure wall, i.e. the turbulence sweep events in the pressure wall region. Due to the solid wall confinement, the sweep events induce two flows with opposite sign spanwise velocity in the pressure wall region. This dynamic process is responsible for the turbulence energy redistribution from the streamwise component to the spanwise, termed splattering or impingement effect of high-speed fluid[25]. The process is the mechanism to generate the spanwise velocity fluctuation. As shown in fig. 9(a), the enhancement of the splattering effect due to the system rotation is the reason of the increase in the spanwise turbulence intensity in fig. 3(d). The contours in figs. 8(b) and 9(b) show that the system rotation suppresses the splattering effect, hence decreases the generation of the spanwise velocity fluctuation near the suction wall. Thus, the spanwise turbulence intensity is suppressed in the suction wall region of the rotating channel.

5 Concluding remarks

In this study, a nonlinear SGS model, which is consistent with the principle of AMFI, is proposed, and the model coefficients are determined dynamically based on the

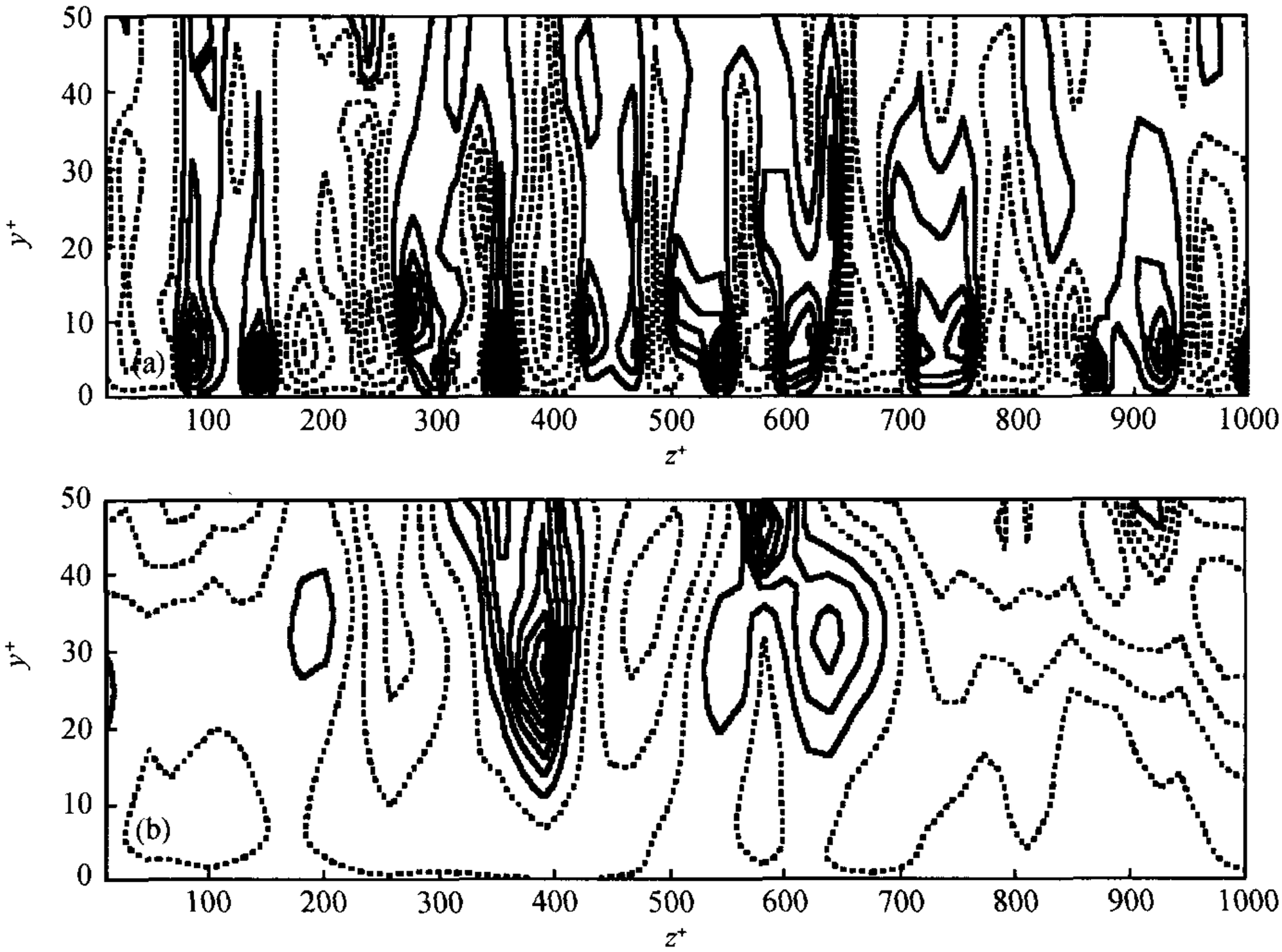

Fig. 9. Contours of the streamwise velocity fluctuation in the y^+–z^+ plane at $N = 0.5$ with the increment of contour 0.5. (a) Near the pressure wall; (b) near the suction wall.

resolved scale motions. The results calculated by using this new dynamic SGS model is proved to be in good agreement with DNS data. Then, turbulence characteristics of the spanwise rotating turbulent channel flow are investigated. The skewness and flatness factors indicate that the turbulence becomes more intermittent near the suction wall. According to the budgets of resolved Reynolds stresses, turbulence production, dissipation and diffusion are enhanced in the pressure wall region. The budget terms in the resolved Reynolds stresses are suppressed evidently in the suction wall region. The flow structures near the pressure wall show that the turbulence sweep and ejection events become more active and the generation of the streamwise vortices is agitated due to the enhancement of splattering effect induced by the rotation effect.

Acknowledgements This work was supported by the National Natural Science Foundation of China (Grant Nos. 10302028 and 10125210), the China NKBRSF Project (Grant No. 2001CB409600), the Hundred Talents Programme of the Chinese Academy of Sciences, and Specialized Research Fund for the Doctoral Program of Higher Education (Grant No. 20020358013).

References

1. Speziale, C. G., Younis, B. A., Rubinstein, R. et al., On consistency conditions for rotating turbulent flows, Phys Fluids, 1998, 22: 2108—2110.
2. Greenspan, H. P., The Theory of Rotating Fluids, Cambridge: Cambridge University Press, 1968.
3. Bradshaw, P., The analogy between streamline curvature and buoyancy in turbulent shear flow, J. Fluid Mech., 1969, 36: 177—191.
4. Fu, S., Wang, C., Second-moment closure modeling of turbulence in a non-inertial frame, Fluid Dynamics

Research, 1997, 20: 43—65.
5. Rubinstein, R., Zhou, Y., The dissipation rate transport equation and subgrid-scale models in rotating turbulence, NASA/CR-97-206250, ICASE Report No.97-63, 1997.
6. Speziale, C. G., Some interesting properties of two-dimensional turbulence, Phys. Fluids, 1981, 24: 1425—1427.
7. Speziale, C. G., Closure models for rotating two-dimensional turbulence, Geophys. Astrophys. Fluid Dynamics, 1983, 23: 69—84.
8. Speziale, C. G., Subgrid scale stress models for the large-eddy simulation of rotating turbulent flows, Geophys. Astrophys. Fluid Dynamics, 1985, 33: 199—222.
9. Shimomura, Y., A family of dynamic subgrid-scale models consistent with asymptotic material frame indifference, J. Phys. Soc. Japan, 1999, 68: 2483—2486.
10. Kobayashi, H., Shimomura, Y., The performance of dynamic subgrid-scale models in the large eddy simulation of rotating homogeneous turbulence, Phys. Fluids, 2001, 13: 2350—2360.
11. Smagorinsky, J., General Circulation experiments with the primitive equations. I. The basic experiment, Mon. Weather Rev., 1963, 91: 99—112.
12. Germano, M., Piomelli, U., Moin, P. et al., A dynamic subgrid-scale eddy viscosity model, Phys. Fluids, 1991, A3: 1760—1765.
13. Zang, Y., Street, R. L., Koseff, J. R., A dynamic mixed subgrid-scale model and its application to turbulent recirculation flows, Phys. Fluids, 1993, A5: 3186—3196.
14. Kosovic, B., Subgrid-scale modelling for the large-eddy simulation of high-Reynolds-number boundary layers, J. Fluid Mech., 1997, 336: 151—182.
15. Lilly, D. K., A proposed modification of the Germano subgrid-scale closure method, Phys. Fluids, 1992, A4: 633—635.
16. Rai, M. M., Moin, P., Direct simulations of turbulent flow using finite-difference schemes, J. Comput. Phys., 1991, 96: 15—53.
17. Kim, J., Moin, P., Application of a fractional-step method to incompressible Navier-Stokes equations, J. Comput. Phys., 1985, 59: 308—323.
18. Kim, J., Moin, P., Moser, R., Turbulence statistics in fully developed channel flow at low Reynolds number, J. Fluid Mech., 1987, 177: 133—166.
19. Kristoffersen, R., Andersson, H. I., Direct simulations of low-Reynolds-number turbulent flow in a rotating channel, J. Fluid Mech., 1993, 256: 163—197.
20. Johnston, J. P., Haleen, R. M., Lezius, D. K., Effects of spanwise rotation on the structures of two-dimensional fully developed turbulent channel flow, J. Fluid Mech., 1972, 26: 533—557.
21. Johnston, J. P., The suppression of shear layer turbulence in rotating systems, ASME J. Fluids Engng., 1973, 195: 229—236.
22. Orlandi, P., Fatica, M., Direct simulations of turbulent flow in a pipe rotating about its axis, J. Fluid Mech., 1997, 343: 43—72.
23. Mansour, N. N., Kim, J., Moin, P., Reynolds-stress and dissipation-rate budgets in a turbulent channel flow, J. Fluid Mech., 1988, 194: 15—44.
24. Runstadler, P. W., Kline, S. J., Reynolds, W. C., An investigation of the flow structure of the turbulent boundary layer, Dept. Mech. Engng., Stanford Univ, Rept MD-8, 1963.
25. Moin, P., Kim, J., Numerical investigation of turbulent channel flow, J. Fluid Mech., 1982, 118: 341—377.